Rydberg-State Engineering: Investigations of Tuning Schemes for Continuous Frequency Sensing

Samuel Berweger,[1] Nikunjkumar Prajapati,[1] Alexandra B. Artusio-Glimpse,[1] Andrew P. Rotunno,[1] Roger Brown,[1] Christopher L. Holloway,[1,*] Matthew T. Simons,[1,†] Eric Imhof,[2] Steven R. Jefferts,[2] Baran N. Kayim,[3] Michael A. Viray,[3] Robert Wyllie,[3] Brian C. Sawyer,[3] and Thad G. Walker[4]

[1] *National Institute of Standards and Technology, Boulder, Colorado 80305, USA*
[2] *Northrop Grumman, Woodland Hills, California 91361, USA*
[3] *Georgia Tech Research Institute, Atlanta, Georgia 30332, USA*
[4] *Department of Physics, University of Madison-Wisconsin, Madison, Wisconsin 53706, USA*

(Received 23 September 2022; revised 16 January 2023; accepted 27 February 2023; published 18 April 2023)

On-resonance Rydberg atom–based radio-frequency- (rf) electric-field sensing methods remain limited by the narrow frequency-signal detection bands available from resonant transitions. An additional rf tuner field can be used to dress or shift a target Rydberg state to return a detuned signal field to resonance and thus dramatically extend the frequency range available for resonant sensing. Here we investigate three distinct tuning-level schemes based on adjacent Rydberg transitions, which are shown to have distinct characteristics and can be controlled with the frequency or the strength of the tuning field. We further show that a two-photon Raman peak can be used as an effective tuning feature separate from conventional Autler-Townes splitting. We compare our tuning schemes with ac Stark effect–based broadband rf-field sensing and show that although the sensitivity is diminished with tuning away from a resonant state, it nevertheless can be used in configurations where there is a low density of Rydberg states, which would result in a weak ac Stark effect.

DOI: 10.1103/PhysRevApplied.19.044049

I. INTRODUCTION

Rydberg-atom sensors have emerged as a promising quantum sensing technology for detecting electric fields (E) in the megahertz-to-gigahertz range [1]. The electric fields couple to a resonant transition between two Rydberg states [2], and the resulting effect on one of these states is measured via the electromagnetically induced transparency (EIT) detected using a two-photon ladder scheme that couples to this state [3–5]. In contrast to traditional antennas, the atom-sensor size can be independent of the radio-frequency (rf) wavelength used, and the atoms themselves do not significantly perturb propagating fields. The full realization of the potential of Rydberg atoms for rf-field sensing for communication and data-transfer applications will require simultaneous high-data-rate bandwidth [6–11], high sensitivity [12–15], and frequency multiplexing.

Rydberg electric field sensing is typically performed using a mixer configuration, where a rf local oscillator (LO) is used to generate a known intermediate frequency from the signal, which dramatically increases the sensitivity [12–14] while simultaneously providing frequency selectivity. The broadband detection of nonresonant fields is readily possible on the basis of the ac Stark shift [16–18], albeit at the cost of reduced sensitivity compared with resonant field sensing [19]. Although resonant Autler-Townes (AT) splitting–based field sensing can achieve sensitivity as high as approximately 5 $\mu V/m\sqrt{Hz}$ [12–14], it is sensitive only to rf fields resonant with discrete dipole-allowed Rydberg transitions that are adjacent to the optically coupled state, and thus is of limited utility for wideband sensing and multiplexing. A recently demonstrated way to increase the spectral range over which resonant Rydberg sensing can be used is to engineer the available Rydberg states—and thus available transitions—using an additional "tuner" rf field [20]. By use of this tuner field to, for example, shift a target Rydberg state via AT splitting to return a detuned signal field to resonance, the sensitivity can be increased.

The continuous range of Rydberg states in terms of the principal and angular momentum quantum numbers [21] can provide a broad manifold of available states for a given signal and tuner frequency of interest. Therefore, a wide range of possible arrangements of the tuner

*christopher.holloway@nist.gov
†matthew.simons@nist.gov

and signal fields—tuning schemes—is available, each with characteristic tuning behavior and associated benefits and drawbacks. In this work, we investigate three possible arrangements of tuner and signal fields, including one described previously [20], which we here term "sequential tuning," as well as two additional schemes, termed "split tuning" and "inverted-sequence tuning." On the basis of the arrangements of these tuning schemes, different spectral tuning features may be available, including avoided crossings of the AT-split peaks as well as an EIT feature arising from a two-rf-photon Raman transition. The tuning control parameter can be either the frequency or the strength of the tuning field.

II. EXPERIMENTAL PROCEDURE

Our experimental setup is based on the cesium two-photon-EIT ladder scheme shown in Fig. 1(a), which has found widespread application in Rydberg electrometry [13, 22–24]. Electric fields are sensed via the Autler-Townes splitting of the Rydberg state by an adjacent rf transition. Our electric field detection is based on the Rydberg-atom-mixer approach introduced in Ref. [25]. Typically, an applied LO is detuned from the signal field of interest by approximately 10 kHz, and the resulting atom-mixed EIT beat frequency (beat note) is then demodulated via lock-in detection. It is inherently challenging to achieve perfect frequency synchronization in simultaneous sweeping of the LO and signal frequencies. To avoid resulting errors, unless otherwise noted, we use amplitude modulation of the LO field to generate the carrier and sideband to simulate the heterodyne/superheterodyne Rydberg-mixer configuration.

To enable direct comparison between the different tuning schemes, we use the same $56D_{5/2}$-$54F_{7/2}$ transition for our LO/signal field in all cases, as illustrated in Fig. 1(b). This transition manifold is chosen to leverage the high linearity of the *D*-*F* transitions [23] and the absence of nearby transition frequencies as is the case for, for example, the *S*-*P* transitions [26]. Our tuning schemes are arranged by optical excitation to either the 56*D* state or the 57*D* state and tuning with either the 53*F*-56*D* transition or the 54*F*-57*D* transition. The corresponding state arrangements for our split-tuning, sequential-tuning, and inverted-sequence-tuning schemes are shown in Figs. 1(c)–1(e), respectively.

The coupler and probe laser beams are sent through a Cs vapor cell in a counterpropagating direction, and the EIT probe and reference intensity beams are detected with use of a balanced photdodiode as illustrated in Fig. 2(a). The rf fields are applied by means of a horn antenna covering the frequency range from 18 to 26.5 GHz with all optical and rf fields copolarized orthogonal to the plane of propagation. Importantly, our choice of rf transitions allows us to use the same horn for all signal/LO/tuner fields, ensuring that all fields are copropagating and optimally overlapped.

Although both the ac Stark shift and AT splitting can be described as Stark shifts, the former represents a nonresonant case with a square dependence on the rf electric field, while the latter is resonant and exhibits a linear dependence on the incident rf field. The ac Stark shift represents an established path and a baseline for broadband Rydberg atom–based field sensing [17,18]. The nonresonant ac Stark shift of the 56*D* EIT peak is shown in Fig 2(b) as a function of LO frequency. The field strength is set to 31 V/m at the resonant 24.7-GHz 56*D*-53*F* transition, and the output power is held constant throughout this sweep. We expect significant variations in field strength within the vapor cell over the frequency range measured due to the frequency-dependent standing-mode profile. These variations have been shown to range from a few percent to more than 70% [4,27]. This is further influenced by effects such as beam positioning and the amount of deposited cesium on the cell walls.

The resonant AT splitting of the $56D_{5/2}$ EIT peak due to a rf field applied at the 56*D*-53*F* tuning transition at 24.7 GHz is shown in Fig 2(c). We use an amplifier to generate large tuner fields greater than 120 V/m to yield Rabi frequencies $\Omega_t/2\pi > 2$ GHz. The AT splitting of

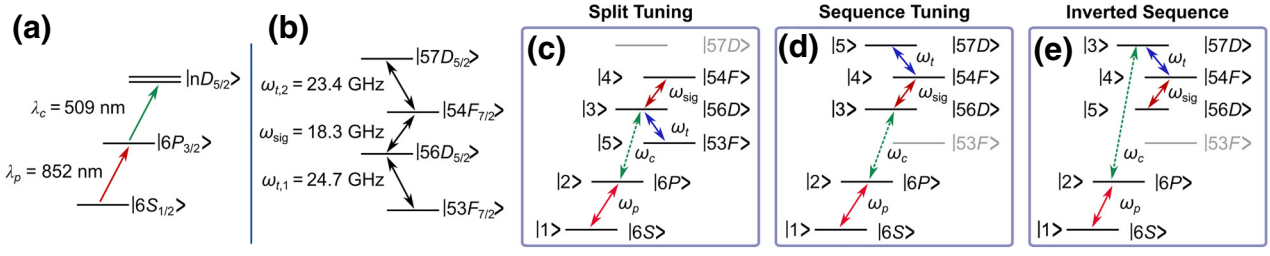

FIG. 1. (a) The Cs EIT ladder scheme to access (b) the Rydberg-state manifold used. In all cases we use the 56*D*-54*F* rf transition for our signal field. We explore three different tuning configurations by means of optical excitation to either the 56*D* state or the 57*D* state and tuning with either the 53*F*-56*D* transition or the 54*F*-57*D* transition. The state arrangements are shown for the split-tuning (c), sequential-tuning (d), and inverted-sequence-tuning (e) schemes. State numbers in (c)–(e) correspond to the five-level models described in Appendix A.

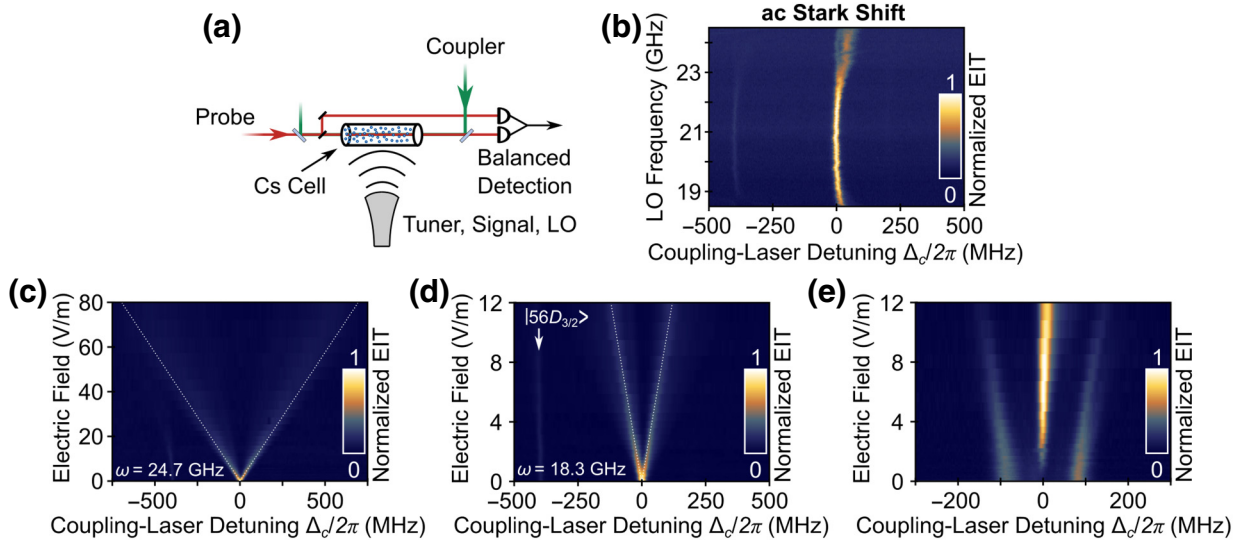

FIG. 2. (a) The experimental setup with counterpropagating probe and coupler beams and the orthogonal horn antenna that is used to broadcast all rf fields used. (b) Shift of the 56D EIT peak due to the ac Stark shift induced by the LO field of differing frequency. The resonant 56D-54F and 56D-53F transitions are just out of view below and above the image, respectively. (c) AT splitting of the 56D EIT peak with a rf field applied to the 56D-53F tuning transition at 24.7 GHz and with (d) the splitting of the same peak in response to a rf field applied to the 56D-54F signal/LO transition at 18.3 GHz. The dashed lines are a guide for the eye. (e) With the coupling-laser frequency set to the resonance frequency of the 57D state and a constant rf field of strength $\Omega/2\pi = 180$ MHz applied to the 57D-54F transition ($f = 23.4$ GHz), we see the emergence of a two-rf-photon Raman peak at $\Delta_c = 0$ as the strength of the second rf field on the 54D-56F transition at $f = 18.3$ GHz is increased.

the same peak due to a field applied on the 56D-54F signal/LO transition at 18.3 GHz is shown in Fig. 2(d). For the signal/LO transitions, we achieve more-moderate maximum fields on the order of 15 V/m. Also shown is the EIT peak due to the $56D_{3/2}$ transition at $\Delta_c/2\pi = -396$ MHz that we use to set our laser-scanned-frequency axis.

Lastly, in Fig. 2(e) we show the effect of two simultaneously applied rf fields producing an EIT peak due to a two-photon Raman transition, which we term the "Raman peak." Here, the coupling laser is resonant with the 57D EIT peak, and we apply a constant rf field of strength $\Omega/2\pi = 180$ MHz set to the 57D-54F transition at $f = 23.4$ GHz that produces the AT doublet. As we increase the strength of the second rf field at $f = 18.3$ GHz on the 54F-56D transition, we see the emergence of an EIT-peak feature near $\Delta_c = 0$. This feature is due to a two-rf-photon Raman transition between the 57D state and the 56D state. We base this conclusion on the observation that we see this peak when $\Delta_t = -\Delta_{\rm sig}$ for our signal/tuner arrangement, i.e., the sum of the photon energies matches that of the 56D-57D transition (see also the discussion of the inverted-sequence scheme below, as well as Appendix B). Also, in our previous work we observed a residual EIT peak at $\Delta_c = 0$ with two resonant rf fields applied, which we attributed to transitions between magnetic sublevels that are forbidden with the π transitions induced by our linear polarization [26]. However, here our EIT-peak structure can be reproduced by our numerically solved five-level model as well as an analytical three-level model (see Appendixes A and B) without the need for additional magnetic sublevels or angular-momentum states. As this Raman peak originates from a two-rf-photon transition adjacent to the optically coupled Rydberg state, it is not observed in the split-tuning case. It is notable that this EIT feature was not observed in comparable two-rf-photon schemes driven by a single rf field [28,29].

III. RESULTS

A. Split tuning

We begin by discussing the conceptually simple split-tuning scheme schematically described in Fig. 3(a). We use the strength of the tuner field (Ω_t) as the control parameter to return a signal field for a given $\Delta_{\rm sig}$ to resonance, which we refer to as "power tuning." The signal and tuning fields are both adjacent to the optically coupled state—56D in this case. We use the tuning field to induce AT splitting of the target state (56D) and the signal/LO fields are returned to resonance when one of the resulting peaks matches the detuned signal/LO frequencies and coupler frequencies:

$$\Omega_t/2 = |\Delta_{\rm sig}| \quad \text{and} \quad \Delta_{\rm sig} = -\Delta_c. \tag{1}$$

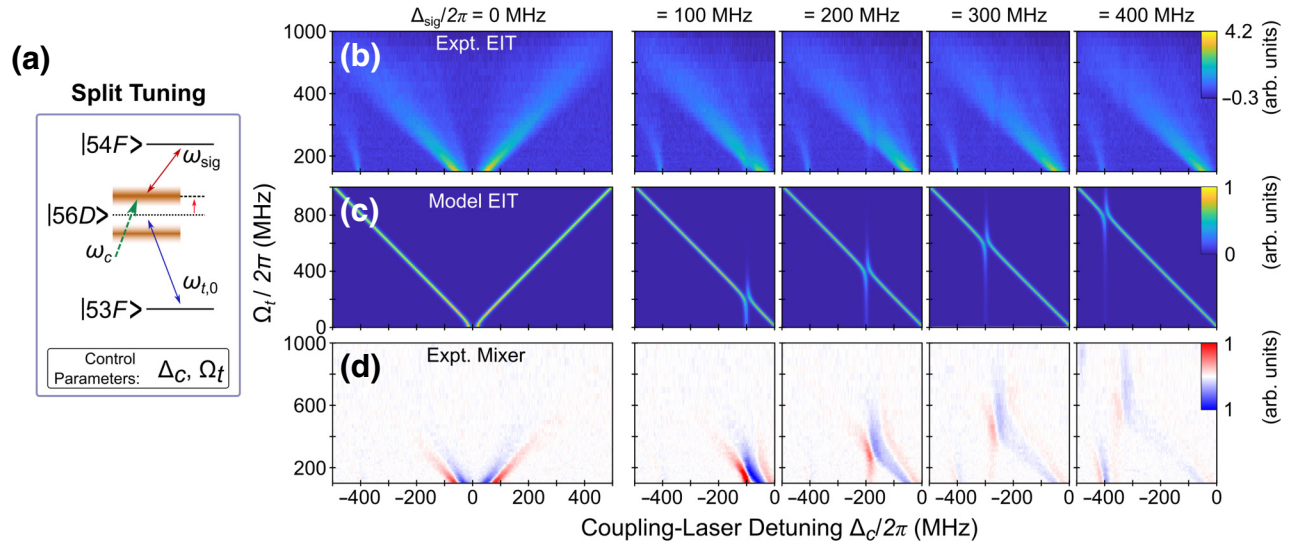

FIG. 3. (a) The states used for power tuning in the split-tuning scheme. (b) False-color plots of the experimental EIT as a function of the tuner Rabi frequency and the coupling-laser detuning, with different values of signal-frequency detuning for each plot indicated. (c) The corresponding modeled EIT shows the location of the tuning peaks obtained, which are clearly visible in (d) the Rydberg-mixer plots.

The measured and modeled EIT spectra are shown in Figs. 3(a) and 3(b), respectively, as a function of Ω_c with $\Omega_{sig}/2\pi = 30$ MHz and Δ_{sig} indicated. The details of the model are presented in Appendix A. The experimental traces appear similar and are dominated by the tuner-induced AT splitting with the residual signal field–induced AT splitting at weak tuner field strengths clearly seen in the model. The modeled data show an avoided crossing—the tuning feature of interest—that appears near the condition where $\Delta_{sig} = -\Delta_c = \Omega_t/2$. These features are also seen in the experimental EIT traces, although they are less well defined due to peak broadening not present in the model. These tuning features can be more-readily resolved using amplitude modulation as shown in Fig. 3(d), which also serves to underscore the practical implications of using a tuning scheme.

For large signal-field-detuning values greater than 150 MHz, we see the benefits of the tuning scheme relative to the residual EIT signal with no applied tuning field or laser detuning. Although the models clearly show the expected behavior of Eq. (1), we find experimentally that this is not the case for our choice of states and that $\Delta_{sig} > \Delta_c$. We attribute this primarily to the presence of the $56D_{3/2}$ transition, which is clearly visible at $\Delta_c/2\pi = -396$ MHz. Because of the simultaneous presence of both the $56D_{3/2}$ state and the dressed $56D_{5/2}$ state for $\Delta_c/2\pi \approx 400$ MHz, the resulting mixing shifts the position of the dressed state. While we show an illustrative tuning range of only 400 MHz here, we note that arbitrarily large tuning ranges are possible in principle, but they are practically limited by peak broadening at larger tuner field strengths.

B. Sequential tuning

We now turn to the previously considered case of sequential tuning [20]. Sequential tuning as shown here can operate using two control parameters as schematically shown in Fig. 4(a). On one hand, power tuning can readily be used, where we hold $\Delta_t = 0$ and increase Ω_t to control the amount of induced AT splitting. However, it also allows the use of two distinct frequency-tuning features. In one case it involves frequency tuning using the Raman-peak feature. If Ω_t is kept constant, we can also use Δ_t as the control parameter to keep the signal field on a resonance by tracking the Ω_t-dependent signal maxima.

The power tuning is shown in the false-color plots of the experimental EIT shown in Fig. 4(b) and the corresponding mixer signal in Fig. 4(c). Here the signal field links the optically coupled $56D$ state to the $54F$ state, while the tuner field applied to the $54F$-$57D$ transition is used to split and tune the energy levels of the $54F$ state. For these plots we lock the coupling laser to the EIT maximum and sweep Δ_{sig} while increasing Ω_t and maintaining $\Delta_t = 0$. The tuner-induced splitting of the $54F$ state can clearly be seen as providing a means to return the detuned signal field to resonance.

The more-general utility of sequential tuning is shown in Figs. 4(d)–4(f), showing the experimental EIT, the modeled EIT, and the experimental mixer signals, respectively, as a function of Δ_{sig} and Δ_t for the tuner Rabi frequencies indicated. Here the coupling laser is again locked to the $56D$ EIT maximum, giving rise to an overall large transparency. At low tuner Rabi frequencies, the effect of the tuner field is limited, and the EIT behavior is

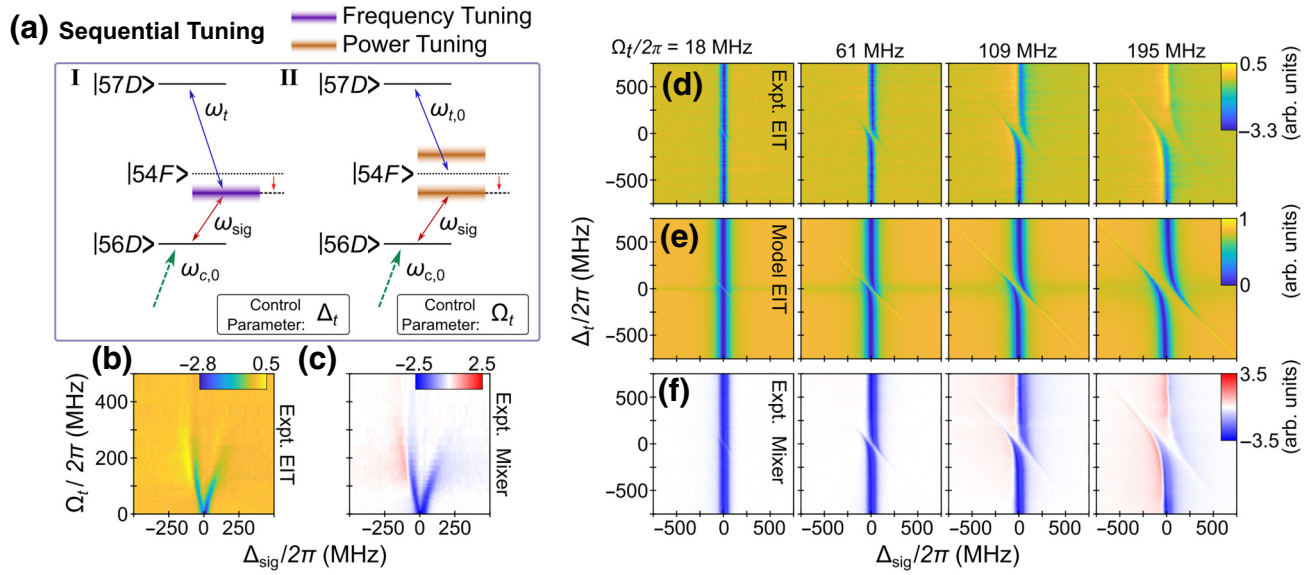

FIG. 4. (a) The tuning schemes used in the sequential arrangement. Experimental EIT (b) and mixer (c) plots of power tuning. The signal field is set to the resonant 56*D*-54*F* transition and the tuning field is applied to the 54*F*-57*D* transition with increasing strength, inducing the observed AT splitting in the 54*F* state. A set of false-color plots of sweeps of Δ_t and Δ_{sig} showing the experimental EIT (d), the modeled EIT (e), and the experimental mixer data (f) as a function of increasing tuner field strength.

dominated by reduced transparency resulting from the signal field–induced AT splitting near $\Delta_{sig} = 0$. As the tuner Rabi frequency is increased, it AT splits the 54*F* state, and the resulting dressed states are seen as ω_{sig} is swept. At large values of Ω_t, the ω_{sig}-dependent EIT peaks begin shifting and the mixer signal becomes asymmetric due to the ac Stark effect.

One further feature of note is seen in Figs. 4(d)–4(f). A feature of increased EIT is seen for $\Delta_t = -\Delta_{sig}$ in the model results, which is not clearly seen in the experimental EIT but is apparent in the mixer signal. This EIT feature is due to the Raman peak shown in Fig. 2(e), which is discussed in further detail in the next section.

C. Inverted-sequence tuning

We now turn to the last of the three tuning schemes addressed in this work, inverted-sequence tuning. Although it is conceptually similar to the sequential-tuning arrangement, reversing the order of the signal and tuning fields has significant consequences for the tuning mechanisms available and their efficacy. To maintain consistency and enable a direct comparison with the other tuning schemes, we maintain the 56*D*-54*F* signal transition and the 57*D*-54*F* tuner transition as illustrated in Fig. 5(a). We invert the sequence by changing the coupling-laser frequency to probe the 57D state. With the tuner transition adjacent to the optically coupled state, we can use fields stronger than those desirable for the LO, so as to leverage the benefits of large Rabi rates and associated AT splitting. On one hand, as further discussed below, we can apply large values of Ω_t to effectively split the 57*D* EIT peak to access the Raman-peak feature for frequency tuning. On the other hand, the inverted-sequence scheme also readily lends itself to power tuning comparable to the split-tuning scheme discussed above.

Power tuning in the inverted-sequence scheme is shown in Figs. 5(b)–5(d). Since we establish the baseline utility of power tuning in Fig. 3, we show a larger coupling-laser-frequency range here to illustrate a few key features and differences. First, because of the arrangement of the states used, we find for our inverted-sequence scheme here that negative Δ_{sig} is tuned into resonance at negative values of Δ_c. Secondly, the Raman peak is seen at $\Delta_c = \Delta_{sig} = 0$ in the experimental and modeled EIT, as well as the mixer signal. This feature is weak, but is identified by the black arrows and the white arrow. Since we show larger values of Δ_c here, two tuning peaks become visible, where we note that similar peaks would also be seen in the split-tuning case. These arise from two distinct signal transitions: the 56*D*-54*F* transition of interest, and the 55*F*-57*D* transition at $\omega_{sig} = 17.4$ GHz that is simultaneously measured in the split-tuning scheme. Although our interest here is in the 56*D*-54*F* signal transition, the simultaneous presence of an additional signal arising from a split-tuning scheme provides a direct comparison. With a difference in transition dipole moments of less than 5%, the equivalent signal levels achieved in the peaks at $\Delta_{sig} = -600$ MHz and $\Delta_{sig} = -400$ MHz reflect the result that the three-level Hamiltonians produce the same eigenvalues for both these schemes when $\Delta_t = 0$ (see Appendix B). As in the split-tuning scheme, in contrast to the models, we again find that

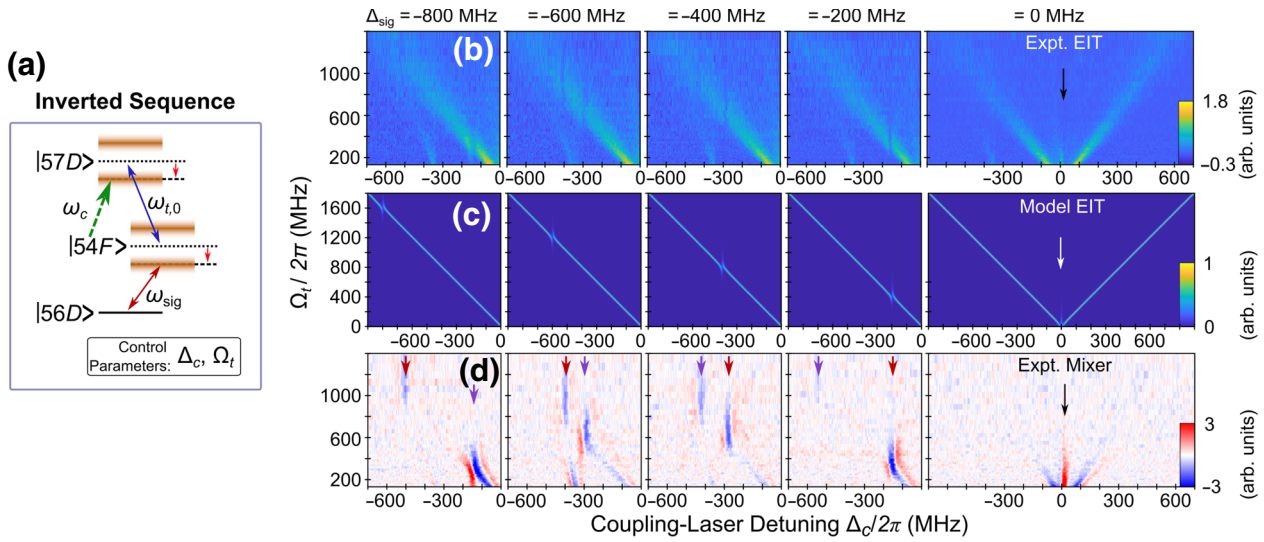

FIG. 5. (a) Power tuning in the inverted-sequence scheme. False-color plots of power tuning using the inverted-sequence scheme with the experimental raw EIT signal (b), the modeled EIT signal (c), and the mixer signal (d). The red arrows in (d) indicate EIT features due to the 56*D*-54*F* transition, while the violet arrows indicate EIT features arising from the 57*D*-55*F* transition. Note different *x*-axis scaling between experimental and modeled data. The black arrows and the white arrow indicate the position of the Raman peak.

$|\Delta_{sig}| > \Delta_c$. We note that this is not generally the case, and in the absence of a fine-structure peak, these two values remain equal in magnitude.

The inverted-sequence scheme also provides an opportunity to use the Raman peak discussed previously and schematically shown in Fig. 6(a). False-color plots of frequency tuning with the coupling laser locked to the EIT maximum are shown in Figs. 6(b)–6(d). Although we show a range of ±1 GHz in tuning in the modeled EIT in Fig. 6(c), the experimental EIT in Fig. 6(b) and the mixer signals in Fig. 6(d) are shown only for $\Delta_{sig} > -600$ MHz because the signal becomes dominated by the resonant 57*D*-55*F* transition at $\Delta_{sig} \approx -900$ MHz. The residual nonresonant background seen in the mixer signal is due to this transition via the ac Stark effect, which is further influenced by the tuner at higher field strengths. With the laser locked to the maximum of the 57*D* EIT peak, the primary effect of the tuner field is AT splitting of the peak,

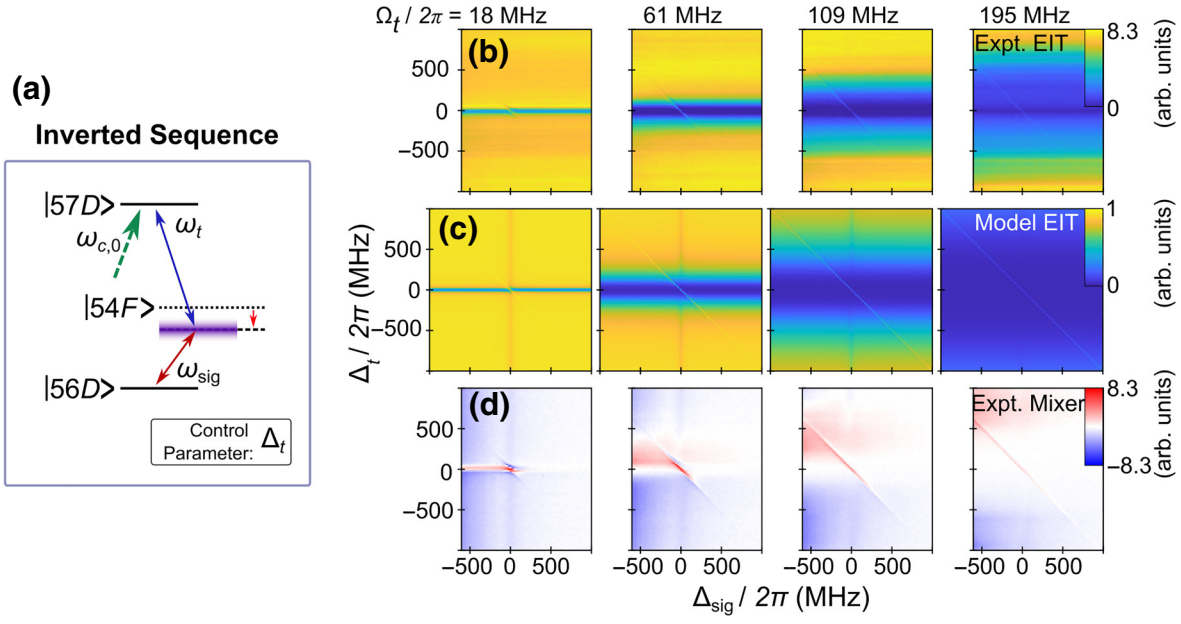

FIG. 6. (a) Frequency tuning in the inverted-sequence scheme. False-color plots of frequency tuning using an inverted sequence with the experimental EIT (b), the modeled EIT (c), and the experimental mixer signal (d).

reducing the overall EIT maximum. At low tuner coupling frequency, the induced splitting is small and the magnitude is limited for small values of Δ_t. As Ω_t increases, however, the values of Δ_t affected by the AT splitting increase.

The tuning-relevant feature seen in all traces in Fig. 6 is the increased EIT amplitude on the diagonal, where $\Delta_{\text{sig}} = -\Delta_t$, corresponding to the Raman feature seen in Fig. 2(e). As seen in the modeled-EIT plots, this feature persists over a broad range of frequency detuning largely independent of Ω_t. However, in practice—as seen in both the experimental-EIT and the experimental-mixer-signal plots—the tunability of this feature is limited and increases with Ω_t. This is because this Raman feature is weaker than the resonant EIT peak, and therefore becomes discernible only once the EIT peak is sufficiently split to separate it from the Raman peak of interest. As a consequence, larger values of Δ_{sig} require increasingly large values of Ω_t. The mixer signal clearly reveals the inherent broadband tunability of the frequency tuning in the inverted-sequence scheme, but unless the Raman peak is clearly distinguished from the resonant EIT peak, residual ac Stark effects from nearby transitions can interfere with signal detection. The mixer data at $\Omega_t/2\pi = 195$ MHz also caution that the magnitude of the Raman peak–based tuning scheme is approximately comparable to that of the nonresonant background arising from the ac Stark effect.

D. Sensitivity comparison

We provide a direct comparison between tuning schemes by performing baseline sensitivity measurements using a Rydberg mixer using two separately sourced signals detuned by a beat-note frequency of 11.2 kHz. All measurements are acquired with the coupling laser tuned to the 56D transition used throughout this work. The Rydberg-mixer signal is shown in Fig. 7(a) as a function of the signal field strength, E_{sig}, for on-resonant AT-based field sensing, the Raman peak, and off-resonant ac Stark sensing at 21.5 GHz [see Fig. 2(b)]. Also shown are the measurement noise floor (dashed line) calculated as the mean of the data points below the detection threshold that represent the measurement noise and the signal amplitude corresponding to a signal-to-noise ratio of 1. Alternatively, the noise floor could be characterized using a spectrum analyzer. We emphasize that throughout the measurements for the sensitivity comparison, we are careful to maintain consistent experimental conditions to enable a direct comparison.

We use a lock-in time constant τ of 1 s, resulting in a bandwidth of $1/2\pi\tau$. Thus the on-resonant sensitivity here is approximately 300 $\mu\text{V/m}\,\text{Hz}^{-1/2}$ As expected, the on-resonant mixer provides the highest sensitivity, approximately 3 times greater than the Raman peak, which is in turn twice as sensitive as the ac Stark effect. It is important to note that although the ac Stark effect here is measured

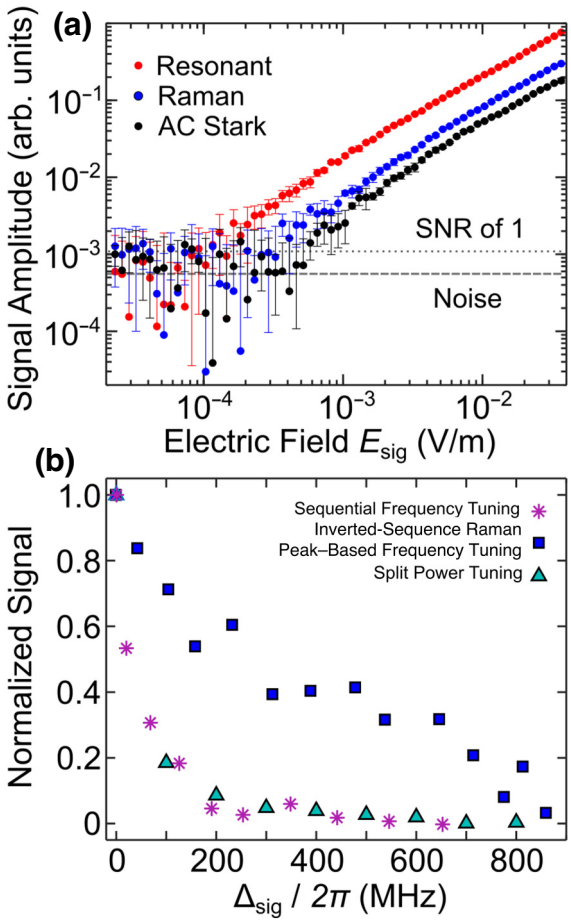

FIG. 7. (a) Comparison of the baseline sensitivity of on-resonance detection on the 56D-54F transition, the Raman EIT peak, and the ac Stark shift at 21.5 GHz. (b) Roll-off of the mixer signal for the different tuning mechanisms: split-scheme power tuning (cyan triangles), sequential-scheme frequency tuning (magenta stars), and inverted-sequence Raman peak–based frequency tuning (blue squares). SNR, signal-to-noise ratio.

far-detuned from resonance, it is nevertheless in a frequency range with a large manifold of D-F transitions. We expect that the relative sensitivity will be lower in a spectral range where fewer nearby transitions are available, such as at a lower principal quantum number n.

We further explore the roll-off in the measured mixer signal as a function of Δ_{sig}. The mixer signals normalized to their on-resonance values are shown in Fig. 7(b) as a function of Δ_{sig} for split-scheme power tuning [cyan triangles, data from the sequence partly shown in Fig. 3(d)], the inverted-sequence Raman peak for $\Omega_t/2\pi = 195$ MHz [blue squares, data from Fig. 6(d)], and sequential-scheme frequency tuning for $\Omega_t/2\pi = 109$ MHz [magenta stars, data from Fig. 4(f)]. For the inverted tuning scheme we further correct the data by subtracting the background that originates from the ac Stark shift. It can readily be seen that although the sensitivity of the split-scheme power

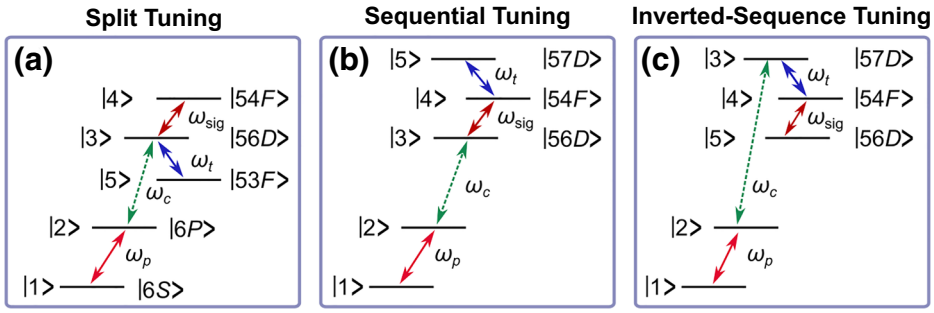

FIG. 8. Level numbers referenced in the master-equation model of each tuning scheme.

tuning and the sequential-scheme frequency tuning rolls off rapidly and diminishes to around 10% of the on-resonant values within 200 MHz of detuning, the inverted-sequence Raman peak diminishes much more slowly, reaching 10% of the peak value at around 800 MHz of detuning.

IV. DISCUSSION

Throughout this work we describe several tuning schemes and mechanisms that can be used to return a detuned signal field to resonance so as to achieve continuous frequency detection. This is done using an additional tuner rf field in addition to the signal/LO fields used for conventional Rydberg-mixer measurements. These tuning mechanisms rely on either the use of tuner field–induced AT splitting of a target state to engineer a resonant signal transition (power tuning) or the use of a two-rf-photon transition to link two real Rydberg states (frequency tuning). In all cases, there is a net loss in sensitivity compared with the on-resonant sensing case. This can be attributed to a distribution of the transition oscillator strength of the bare state into the two AT-split peaks. Further limitations in tuning sensitivity not accounted for in our models include linewidth broadening due to the field inhomogeneity typical of vapor cells and the effects of magnetic sublevels [23].

In all schemes shown here, power tuning leverages tuner field–induced AT splitting. Thus, an overarching challenge presented by power tuning is the large and uniform tuner fields required by the general condition for an on-resonant tuner field that $\Omega_t = 2|\Delta_{sig}|$. For instance, for our states chosen here, a detuning of $\Delta_{sig}/2\pi = 1000$ MHz requires $\Omega_t/2\pi = 2000$ MHz, corresponding to an electric field $E > 100$ V/m. Although we can readily achieve such fields with our setup, most signal generators (including ours) require an additional amplification stage to produce sufficiently high fields with a horn antenna.

Leveraging the Raman peak resulting from the coherent interaction of the tuner and LO fields for field sensing presents an approach here for Rydberg field sensing. This inverted tuning scheme was also explored in recent work [30], although the contribution of a two-photon Raman peak was not reported. As we show in Fig. 7, the overall sensitivity is not significantly diminished compared with the resonant EIT signal, although we note that at low tuner field strengths, where the resonant EIT peak is not fully split, an additional nonresonant EIT response can contribute too. Tuning using the Raman peak also benefits from the comparably slow roll-off of the sensitivity. In terms of practical implementations, a frequency-tuning scheme based on the Raman peak is attractive because it is easier to tune the rf frequencies rather than the laser as required for power tuning.

Lastly, it bears emphasizing that the ac Stark sensitivity remains good and benefits from needing merely an LO field rather than an additional tuner field. However, the required LO fields are typically significantly stronger than those yielding optimal sensitivity in other schemes.

We conclude by noting that we demonstrate a set of tuning schemes that can be used for resonant frequency detection by engineering the Rydberg energy levels to return a detuned signal field to resonance using a tuner field. These include tuner field–induced AT splitting as well as producing a Raman-peak feature that can resonantly link two otherwise dipole-forbidden states. In the present case the benefits relative to an ac Stark-based approach are marginal. However, we must emphasize that the details of the sensitivity depend delicately on all aspects of the Rydberg atoms used, including atomic species as well as the principal and angular-momentum quantum numbers. Our choice of states is driven primarily by the desire to have a manifold of transitions available within the bandwidth of our K-band microwave electronics and horn, which leads to inevitable trade-offs in terms of nearby transition frequencies. Therefore, we do not expect that our results are quantitatively universal, but our experience and modeling suggests that these tuning schemes are generally applicable.

ACKNOWLEDGMENTS

This research was performed with funding from the U.S. Defense Advanced Research Projects Agency. The views, opinions, and/or findings expressed are those of the authors

and should not be interpreted as representing the official views or policies of the U.S. Department of Defense or the U.S. Government. This article is a contribution of the U.S. Government, not subject to U.S. copyright.

APPENDIX A: MASTER-EQUATION MODEL

We use a master-equation model of the EIT signals for the various atomic transition schemes used here. Each of the five states addressed in the split-tuning, sequential-tuning, and inverted- sequence-tuning configurations is labeled in Figs. 1(c)–1(e) for ease of reference. The power of the probe beam measured on the detector (the EIT signal, i.e., the probe transmission through the vapor cell) is given by [31]

$$P = P_0 \exp\left(-\frac{2\pi L \,\mathrm{Im}\,[\chi]}{\lambda_p}\right) = P_0 \exp\left(-\alpha L\right), \quad \text{(A1)}$$

where P_0 is the power of the probe beam at the input of the cell, L is the length of the cell, λ_p is the wavelength of the probe laser, χ is the susceptibility of the medium seen by the probe laser, and $\alpha = 2\pi\,\mathrm{Im}\,[\chi]/\lambda_p$ is Beer's absorption coefficient for the probe laser. The susceptibility for the probe laser is related to the density-matrix component (ρ_{21}) by the following expression [31]:

$$\chi = \frac{2\mathcal{N}_0 \wp_{12}}{E_p \epsilon_0}\rho_{21_D} = \frac{2\mathcal{N}_0}{\epsilon_0 \hbar}\frac{(dea_0)^2}{\Omega_p}\rho_{21_D}, \quad \text{(A2)}$$

where $d = 2.02$ [32] is the normalized transition dipole moment for the probe laser, Ω_p is the Rabi frequency for the probe laser in the unit of radians per second, and e and $\hbar$ are the elementary charge and the reduced Planck constant, respectively. The subscript D on ρ_{21} represents a Doppler-averaged value. $\mathcal{N}_0$ is the total density of atoms in the cell and is given by

$$\mathcal{N}_0 = \frac{p}{k_B T}, \quad \text{(A3)}$$

where k_B is the Boltzmann constant, T is the temperature in kelvins, and the pressure p (in pascals) is given by [32]

$$p = 10^{9.717 - \frac{3999}{T}}. \quad \text{(A4)}$$

In Eq. (A2), $\wp_{12}$ is the transition dipole moment for the $|1\rangle$-$|2\rangle$ transition, ϵ_0 is the vacuum permittivity, and E_p is the amplitude of the probe-laser electric field.

The density-matrix component (ρ_{21}) is obtained from the master equation [31]

$$\dot{\boldsymbol{\rho}} = \frac{\partial \boldsymbol{\rho}}{\partial t} = -\frac{i}{\hbar}[\mathbf{H}, \boldsymbol{\rho}] + \boldsymbol{\mathcal{L}}, \quad \text{(A5)}$$

where $\mathbf{H}$ is the Hamiltonian of the atomic system under consideration and $\boldsymbol{\mathcal{L}}$ is the Lindblad operator, which accounts for the decay processes in the atom. The $\mathbf{H}$ and $\boldsymbol{\mathcal{L}}$ matrices for the three different tuning schemes are given below.

We numerically solve these equations to find the steady-state solution for ρ_{21} for various values of the Rabi frequency (Ω_i) and various detunings (Δ_i). This is done by our forming a matrix with the system of equations for $\dot{\rho}_{ij} = 0$. The null space of the resulting system matrix is the steady-state solution. The steady-state solution for ρ_{21} is then Doppler averaged [31]:

$$\rho_{21_D} = \frac{1}{\sqrt{\pi}u}\int_{-3u}^{3u} \rho_{21}\left(\Delta_p', \Delta_c'\right) e^{(-v^2/u^2)} dv, \quad \text{(A6)}$$

where $u = \sqrt{2k_B T/m}$, where m is the mass of the atom. We use the case where the probe laser beam and coupling laser beam are counterpropagating. Thus, the frequency seen by the atom moving toward the probe beam is upshifted by $2\pi v/\lambda_p$ (where v is the velocity of the atoms), while the frequency of the coupling beam seen by the same atom is downshifted by $2\pi v/\lambda_c$. The probe-beam detuning and the coupling-beam detuning are modified as follows:

$$\Delta_p' = \Delta_p - \frac{2\pi}{\lambda_p}v \quad \text{and} \quad \Delta_c' = \Delta_c + \frac{2\pi}{\lambda_c}v. \quad \text{(A7)}$$

1. Split tuning

For the split-tuning scheme shown in Fig. 1(c), the Hamiltonian can be expressed as

$$\mathbf{H} = \frac{\hbar}{2}\begin{bmatrix} 0 & \Omega_p & 0 & 0 & 0 \\ \Omega_p^* & A & \Omega_c & 0 & 0 \\ 0 & \Omega_c^* & B & \Omega_{\mathrm{sig}} & \Omega_t \\ 0 & 0 & \Omega_{\mathrm{sig}}^* & C & 0 \\ 0 & 0 & \Omega_t^* & 0 & D \end{bmatrix}, \quad \text{(A8)}$$

where Ω_p, Ω_c, Ω_{sig}, and Ω_t are the Rabi frequencies of the probe laser, coupling laser, signal field, and tuner field, respectively, and Ω^* denotes the complex conjugate. Also,

$$\begin{aligned} A &= -2\Delta_p, \\ B &= -2(\Delta_p + \Delta_c), \\ C &= -2(\Delta_p + \Delta_c + \Delta_{\mathrm{sig}}), \\ D &= -2(\Delta_p + \Delta_c - \Delta_t), \end{aligned} \quad \text{(A9)}$$

where Δ_p, Δ_c, Δ_{sig}, and Δ_t are the detunings of the probe laser, the coupling laser, the signal field, and the tuner field, respectively, defined as

$$\Delta_{p,c,\mathrm{sig},t} = \omega_{p,c,\mathrm{sig},t} - \omega_{12,23,34,35}, \quad \text{(A10)}$$

where ω_{12}, ω_{23}, ω_{34}, and ω_{35} are, respectively, the on-resonance angular frequencies of the $|1\rangle$-$|2\rangle$, $|2\rangle$-$|3\rangle$, $|3\rangle$-$|4\rangle$, and $|3\rangle$-$|5\rangle$ transitions, and ω_p, ω_c, ω_{sig}, and ω_t are

the angular frequencies of the probe, coupling, signal, and tuner fields, respectively. Notably in this scheme, $\Delta_t/2\pi = 0$ MHz because the tuning field is locked to the $|3\rangle$-$|5\rangle$ transition. The $\boldsymbol{\mathcal{L}}$ matrix of this system is given as follows:

$$\boldsymbol{\mathcal{L}} = \begin{bmatrix} \Gamma_2\rho_{22} & -\gamma_{12}\rho_{12} & -\gamma_{13}\rho_{13} & -\gamma_{14}\rho_{14} & -\gamma_{15}\rho_{15} \\ -\gamma_{21}\rho_{21} & \Gamma_3\rho_{33} - \Gamma_2\rho_{22} & -\gamma_{23}\rho_{23} & -\gamma_{24}\rho_{24} & -\gamma_{25}\rho_{25} \\ -\gamma_{31}\rho_{31} & -\gamma_{32}\rho_{32} & \Gamma_4\rho_{44} + \Gamma_5\rho_{55} - \Gamma_3\rho_{33} & -\gamma_{34}\rho_{34} & -\gamma_{35}\rho_{35} \\ -\gamma_{41}\rho_{41} & -\gamma_{42}\rho_{42} & -\gamma_{43}\rho_{43} & -\Gamma_4\rho_{44} & -\gamma_{45}\rho_{45} \\ -\gamma_{51}\rho_{51} & -\gamma_{52}\rho_{52} & -\gamma_{53}\rho_{53} & -\gamma_{45}\rho_{45} & -\Gamma_5\rho_{55} \end{bmatrix}, \tag{A11}$$

where $\gamma_{ij} = (\Gamma_i + \Gamma_j)/2$ and $\Gamma_{i,j}$ are the transition decay rates. Since the purpose of the present study is to explore the intrinsic limitations of Rydberg-EIT field sensing in vapor cells, no collision terms or dephasing terms are added. While Rydberg-atom collisions, Penning ionization, and ion electric fields can, in principle, cause dephasing, such effects can, for instance, be alleviated by reducing the beam intensities, lowering the vapor pressure, or limiting the atom-field interaction time. In this analysis we set $\Gamma_1 = 0$, $\Gamma_2 = 2\pi \times (6\text{ MHz})$, $\Gamma_3 = 2\pi \times (3\text{ kHz})$, and $\Gamma_{4,5} = 2\pi \times (2\text{ kHz})$. Note, Γ_2 is for the D2 line in ^{133}Cs [32], and Γ_3, Γ_4, and Γ_5 are typical Rydberg decay rates.

2. Sequential tuning

For the sequential-tuning scheme shown in Fig. 1(d), the Hamiltonian can be expressed as

$$\mathbf{H} = \frac{\hbar}{2}\begin{bmatrix} 0 & \Omega_p & 0 & 0 & 0 \\ \Omega_p^* & A & \Omega_c & 0 & 0 \\ 0 & \Omega_c^* & B & \Omega_{\text{sig}} & 0 \\ 0 & 0 & \Omega_{\text{sig}}^* & C & \Omega_t \\ 0 & 0 & 0 & \Omega_t^* & D \end{bmatrix}, \tag{A12}$$

where Ω_p, Ω_c, Ω_{sig}, and Ω_t are the Rabi frequencies of the probe laser, coupling laser, signal field, and tuner field, respectively. Also,

$$\begin{aligned} A &= -2\Delta_p, \\ B &= -2(\Delta_p + \Delta_c), \\ C &= -2(\Delta_p + \Delta_c + \Delta_{\text{sig}}), \\ D &= -2(\Delta_p + \Delta_c + \Delta_{\text{sig}} + \Delta_t), \end{aligned} \tag{A13}$$

where Δ_p, Δ_c, Δ_{sig}, and Δ_t are the detunings of the probe laser, the coupling laser, the signal field, and the tuner field, respectively, defined as

$$\Delta_{p,c,\text{sig},t} = \omega_{p,c,\text{sig},t} - \omega_{12,23,34,45}, \tag{A14}$$

where ω_{12}, ω_{23}, ω_{34}, and ω_{45} are the on-resonance angular frequencies of the $|1\rangle$-$|2\rangle$, $|2\rangle$-$|3\rangle$, $|3\rangle$-$|4\rangle$, and $|4\rangle$-$|5\rangle$ transitions for the probe, coupling, signal, and tuner fields, respectively, and ω_p, ω_c, ω_{sig}, and ω_t are the angular frequencies of the probe, coupling, signal, and tuner fields, respectively.

The $\boldsymbol{\mathcal{L}}$ matrix of this system is given as follows:

$$\boldsymbol{\mathcal{L}} = \begin{bmatrix} \Gamma_2\rho_{22} & -\gamma_{12}\rho_{12} & -\gamma_{13}\rho_{13} & -\gamma_{14}\rho_{14} & -\gamma_{15}\rho_{15} \\ -\gamma_{21}\rho_{21} & \Gamma_3\rho_{33} - \Gamma_2\rho_{22} & -\gamma_{23}\rho_{23} & -\gamma_{24}\rho_{24} & -\gamma_{25}\rho_{25} \\ -\gamma_{31}\rho_{31} & -\gamma_{32}\rho_{32} & \Gamma_4\rho_{44} - \Gamma_3\rho_{33} & -\gamma_{34}\rho_{34} & -\gamma_{35}\rho_{35} \\ -\gamma_{41}\rho_{41} & -\gamma_{42}\rho_{42} & -\gamma_{43}\rho_{43} & \Gamma_5\rho_{55} - \Gamma_4\rho_{44} & -\gamma_{45}\rho_{45} \\ -\gamma_{51}\rho_{51} & -\gamma_{52}\rho_{52} & -\gamma_{53}\rho_{53} & -\gamma_{45}\rho_{45} & -\Gamma_5\rho_{55} \end{bmatrix}. \tag{A15}$$

Once again $\gamma_{ij} = (\Gamma_i + \Gamma_j)/2$ and $\Gamma_{i,j}$ are the transition decay rates, where $\Gamma_1 = 0$, $\Gamma_2 = 2\pi \times (6\text{ MHz})$, $\Gamma_3 = 2\pi \times (3\text{ kHz})$, and $\Gamma_{4,5} = 2\pi \times (2\text{ kHz})$.

3. Inverted-sequence tuning

For the inverted-sequence scheme shown in Fig. 1(e), the Hamiltonian can be expressed as

$$\mathbf{H} = \frac{\hbar}{2}\begin{bmatrix} 0 & \Omega_p & 0 & 0 & 0 \\ \Omega_p^* & A & \Omega_c & 0 & 0 \\ 0 & \Omega_c^* & B & \Omega_t & 0 \\ 0 & 0 & \Omega_t^* & C & \Omega_{\text{sig}} \\ 0 & 0 & 0 & \Omega_{\text{sig}}^* & D \end{bmatrix}, \tag{A16}$$

where Ω_p, Ω_c, Ω_t, and Ω_{sig} are the Rabi frequencies of the probe laser, coupling laser, tuner field, and signal field,

respectively. Also,

$$\begin{aligned} A &= -2\Delta_p, \\ B &= -2(\Delta_p + \Delta_c), \\ C &= -2(\Delta_p + \Delta_c - \Delta_t), \\ D &= -2(\Delta_p + \Delta_c - \Delta_t - \Delta_{\text{sig}}), \end{aligned} \tag{A17}$$

where Δ_p, Δ_c, Δ_t, and Δ_{sig} are the detunings of the probe laser, coupling laser, tuner field, and signal field, respectively, defined as

$$\Delta_{p,c,t,\text{sig}} = \omega_{p,c,t,\text{sig}} - \omega_{12,23,34,45}, \tag{A18}$$

where ω_{12}, ω_{23}, ω_{34}, and ω_{45} are the on-resonance angular frequencies of the $|1\rangle$-$|2\rangle$, $|2\rangle$-$|3\rangle$, $|3\rangle$-$|4\rangle$, and $|4\rangle$-$|5\rangle$ transitions for the probe, coupling, tuner, and signal fields, respectively, and ω_p, ω_c, ω_t, and ω_{sig} and are the angular frequencies of the probe, coupling, tuner, and signal fields, respectively.

The $\boldsymbol{\mathcal{L}}$ matrix of this system is given as follows:

$$\boldsymbol{\mathcal{L}} = \begin{bmatrix} \Gamma_2\rho_{22} & -\gamma_{12}\rho_{12} & -\gamma_{13}\rho_{13} & -\gamma_{14}\rho_{14} & -\gamma_{15}\rho_{15} \\ -\gamma_{21}\rho_{21} & \Gamma_5\rho_{55} - \Gamma_2\rho_{22} & -\gamma_{23}\rho_{23} & -\gamma_{24}\rho_{24} & -\gamma_{25}\rho_{25} \\ -\gamma_{31}\rho_{31} & -\gamma_{32}\rho_{32} & -\Gamma_3\rho_{33} & -\gamma_{34}\rho_{34} & -\gamma_{35}\rho_{35} \\ -\gamma_{41}\rho_{41} & -\gamma_{42}\rho_{42} & -\gamma_{43}\rho_{43} & \Gamma_3\rho_{33} - \Gamma_4\rho_{44} & -\gamma_{45}\rho_{45} \\ -\gamma_{51}\rho_{51} & -\gamma_{52}\rho_{52} & -\gamma_{53}\rho_{53} & -\gamma_{45}\rho_{45} & \Gamma_4\rho_{44} - \Gamma_5\rho_{55} \end{bmatrix}. \tag{A19}$$

Again $\gamma_{ij} = (\Gamma_i + \Gamma_j)/2$ and $\Gamma_{i,j}$ are the transition decay rates, but this time $\Gamma_1 = 0$, $\Gamma_2 = 2\pi \times (6\ \text{MHz})$, $\Gamma_{3,4} = 2\pi \times (2\ \text{kHz})$, and $\Gamma_5 = 2\pi \times (3\ \text{kHz})$.

APPENDIX B: SIMPLE THREE-LEVEL MODEL

Here we describe a simple three-level model to understand the EIT-peak position in our experiments. We consider three bare Rydberg states in the sequential-tuning arrangement shown in Fig. 1(d), $|I\rangle \equiv |56D\rangle$, $|J\rangle \equiv |54F\rangle$, and $|K\rangle \equiv |57D\rangle$, with two rf fields applied, one at frequency ω_{sig} detuned by Δ_{sig} from the $|I\rangle \rightarrow |J\rangle$ transition, and the other at frequency ω_t detuned by Δ_t from the $|J\rangle \rightarrow |K\rangle$ transition.

These bare states and fields produce three nearly degenerate energy levels. The first is defined by the atom in state $|I\rangle$ with N_{sig} photons at frequency ω_{sig} and N_t photons at frequency ω_t. The second state is defined by the atom in state $|J\rangle$ with $N_{\text{sig}} - 1$ photons at frequency ω_{sig} and N_t photons at frequency ω_t. The third state is defined by the atom in state $|K\rangle$ with $N_{\text{sig}} - 1$ photons at frequency ω_{sig} and $N_t - 1$ photons at frequency ω_t. These states can be labeled

$$\begin{aligned} |i\rangle &= |I, N_{\text{sig}}, N_t\rangle, \\ |j\rangle &= |J, N_{\text{sig}} - 1, N_t\rangle, \\ |k\rangle &= |K, N_{\text{sig}} - 1, N_t - 1\rangle, \end{aligned} \tag{B1}$$

with energies

$$\begin{aligned} E_i &= E_I + N_{\text{sig}}\hbar\omega_{\text{sig}} + N_t\hbar\omega_t, \\ E_j &= E_J + (N_{\text{sig}} - 1)\hbar\omega_{\text{sig}} + N_t\hbar\omega_t \\ &= E_A + \hbar\Delta_{\text{sig}}, \\ E_k &= E_K + (N_{\text{sig}} - 1)\hbar\omega_{\text{sig}} + (N_t - 1)\hbar\omega_t \\ &= E_A + \hbar(\Delta_{\text{sig}} + \Delta_t). \end{aligned} \tag{B2}$$

The Hamiltonian in the rotating-wave approximation is then

$$\begin{aligned} H_{\text{seq}} = E_i &+ \hbar\Delta_{\text{sig}}|j\rangle\langle j| - \hbar(\Delta_{\text{sig}} + \Delta_t)|k\rangle\langle k| \\ &+ \frac{\hbar\Omega_{\text{sig}}}{2}(|j\rangle\langle i| + |i\rangle\langle j|) + \frac{\hbar\Omega_t}{2}(|k\rangle\langle j| + |j\rangle\langle k|), \end{aligned} \tag{B3}$$

which can be rewritten as

$$H_{\text{seq}} = E_i + \hbar \begin{bmatrix} 0 & \Omega_{\text{sig}}/2 & 0 \\ \Omega_{\text{sig}}/2 & -\Delta_{\text{sig}} & \Omega_t/2 \\ 0 & \Omega_t/2 & -\Delta_{\text{sig}} - \Delta_t \end{bmatrix}. \tag{B4}$$

Similarly, we can write the Hamiltonian matrix for the inverted-sequence tuning as

$$H_{\text{inv}} = E_k + \hbar \begin{bmatrix} \Delta_{\text{sig}} + \Delta_t & \Omega_{\text{sig}}/2 & 0 \\ \Omega_{\text{sig}}/2 & -\Delta_t & \Omega_t/2 \\ 0 & \Omega_t/2 & 0 \end{bmatrix}. \tag{B5}$$

Considering the different arrangement of Rydberg states, $|H\rangle \equiv |53F\rangle$, $|I\rangle \equiv |56D\rangle$, and $|J\rangle \equiv |54F\rangle$, and applying

the signal field along $|I\rangle \rightarrow |J\rangle$ and the tuner along $|H\rangle \rightarrow |I\rangle$, we can write the split-tuning case as

$$H_{\text{split}} = E_j + \hbar \begin{bmatrix} \Delta_t & \Omega_t/2 & 0 \\ \Omega_t/2 & 0 & \Omega_{\text{sig}}/2 \\ 0 & \Omega_{\text{sig}}/2 & -\Delta_{\text{sig}} \end{bmatrix}. \quad \text{(B6)}$$

Lastly, we turn to the special case in the sequential-tuning case where $\Delta_{\text{sig}} = -\Delta_t$, which we note is the condition where the Raman EIT peak emerges. In this case, three energy eigenvalues can be calculated:

$$E_{0,\pm} = E_i, E_i + \frac{\hbar}{2}\Big(- \Delta_{\text{sig}} \pm \sqrt{\Omega_{\text{sig}}^2 + \Omega_t^2 + \Delta_{\text{sig}}^2}\Big). \quad \text{(B7)}$$

Here the $E_\pm$ solutions correspond to AT splitting with an effective Rabi frequency $\Omega^2 = \Omega_{\text{sig}}^2 + \Omega_t^2$. However, the third peak, E_0, is fixed in frequency at the location of the main EIT peak and corresponds to the two-photon Raman peak we observe.

[1] A. Artusio-Glimpse, M. T. Simons, N. Prajapati, and C. L. Holloway, Modern rf measurements with hot atoms: A technology review of Rydberg atom-based radio frequency field sensors, IEEE Microw. Mag. **23**, 44 (2022).

[2] A. Osterwalder and F. Merkt, Using High Rydberg States as Electric Field Sensors, Phys. Rev. Lett. **82**, 1831 (1999).

[3] J. A. Sedlacek, A. Schwettmann, H. Kübler, R. Löw, T. Pfau, and J. P. Shaffer, Microwave electrometry with Rydberg atoms in a vapour cell using bright atomic resonances, Nat. Phys. **9**, 819 (2012).

[4] C. L. Holloway, J. A. Gordon, A. Schwarzkopf, D. A. Anderson, S. A. Miller, N. Thaicharoen, and G. Raithel, Sub-wavelength imaging and field mapping via electromagnetically induced transparency and Autler-Townes splitting in Rydberg atoms, Appl. Phys. Lett. **104**, 244102 (2014).

[5] H. Fan, S. Kumar, J. Sedlacek, H. Kübler, S. Karimkashi, and J. P. Shaffer, Atom based RF electric field sensing, J. Phys. B: At., Mol. Opt. Phys. **48**, 202001 (2015).

[6] J. S. Otto, M. K. Hunter, N. Kjærgaard, and A. B. Deb, Data capacity scaling of a distributed Rydberg atomic receiver array, J. Appl. Phys. **129**, 154503 (2021).

[7] Z. Song, H. Liu, X. Liu, W. Zhang, H. Zou, J. Zhang, and J. Qu, Rydberg-atom-based digital communication using a continuously tunable radio-frequency carrier, Opt. Express **27**, 8848 (2019).

[8] C. L. Holloway, M. T. Simons, J. A. Gordon, and D. Novotny, Detecting and receiving phase-modulated signals with a Rydberg atom-based receiver, IEEE Antennas Wirel. Propag. Lett. **18**, 1853 (2019).

[9] R. E. Sapiro, G. Raithel, and D. A. Anderson, Time dependence of Rydberg EIT in pulsed optical and RF fields, J. Phys. B: At., Mol. Opt. Phys. **53**, 094003 (2020).

[10] D. H. Meyer, K. C. Cox, F. K. Fatemi, and P. D. Kunz, Digital communication with Rydberg atoms and amplitude-modulated microwave fields, Appl. Phys. Lett. **112**, 211109 (2018).

[11] S. M. Bohaichuk, D. Booth, and J. Shaffer, in *Quantum Sensing and Nano Electronics and Photonics XVIII*, edited by M. Razeghi, G. A. Khodaparast, and M. S. Vitiello, International Society for Optics and Photonics, Vol. 12009 (SPIE, San Francisco, 2022), p. 120090C.

[12] N. Prajapati, A. K. Robinson, S. Berweger, M. T. Simons, A. B. Artusio-Glimpse, and C. L. Holloway, Enhancement of electromagnetically induced transparency based Rydberg-atom electrometry through population repumping, Appl. Phys. Lett. **119**, 214001 (2021).

[13] M. Jing, Y. Hu, J. Ma, H. Zhang, L. Zhang, L. Xiao, and S. Jia, Atomic superheterodyne receiver based on microwave-dressed Rydberg spectroscopy, Nat. Phys. **16**, 911 (2020).

[14] J. A. Gordon, M. T. Simons, A. H. Haddab, and C. L. Holloway, Weak electric-field detection with sub-1 Hz resolution at radio frequencies using a Rydberg atom-based mixer, AIP Adv. **9**, 045030 (2019).

[15] S. Kumar, H. Fan, H. Kübler, J. Sheng, and J. P. Shaffer, Atom-based sensing of weak radio frequency electric fields using homodyne readout, Sci. Rep. **7**, 42981 (2017).

[16] D. A. Anderson and G. Raithel, Continuous-frequency measurements of high-intensity microwave electric fields with atomic vapor cells, Appl. Phys. Lett. **111**, 053504 (2017).

[17] D. H. Meyer, P. D. Kunz, and K. C. Cox, Waveguide-coupled Rydberg spectrum analyzer from 0 to 20 GHz, Phys. Rev. Appl. **15**, 014053 (2021).

[18] H. Li, J. Hu, J. Bai, M. Shi, Y. Jiao, J. Zhao, and S. Jia, Rydberg atom-based am receiver with a weak continuous frequency carrier, Opt. Express **30**, 13522 (2022).

[19] D. H. Meyer, Z. A. Castillo, K. C. Cox, and P. D. Kunz, Assessment of Rydberg atoms for wideband electric field sensing, J. Phys. B: At., Mol. Opt. Phys. **53**, 034001 (2020).

[20] M. T. Simons, A. B. Artusio-Glimpse, C. L. Holloway, E. Imhof, S. R. Jefferts, R. Wyllie, B. C. Sawyer, and T. G. Walker, Continuous radio-frequency electric-field detection through adjacent Rydberg resonance tuning, Phys. Rev. A **104**, 032824 (2021).

[21] R. Brown, B. Kayim, M. Viray, A. Perry, B. Sawyer, and R. Wyllie, VHF/UHF detection using high angular momentum Rydberg states, ArXiv:2205.12876.

[22] K. C. Cox, D. H. Meyer, F. K. Fatemi, and P. D. Kunz, Quantum-Limited Atomic Receiver in the Electrically Small Regime, Phys. Rev. Lett. **121**, 110502 (2018).

[23] A. Chopinaud and J. Pritchard, Optimal State Choice for Rydberg-Atom Microwave Sensors, Phys. Rev. Appl. **16**, 024008 (2021).

[24] C. L. Holloway, M. T. Simons, J. A. Gordon, A. Dienstfrey, D. A. Anderson, and G. Raithel, Electric field metrology for Si traceability: Systematic measurement uncertainties in electromagnetically induced transparency in atomic vapor, J. Appl. Phys. **121**, 233106 (2017).

[25] M. T. Simons, A. H. Haddab, J. A. Gordon, and C. L. Holloway, A Rydberg atom-based mixer: Measuring the phase of a radio frequency wave, Appl. Phys. Lett. **114**, 114101 (2019).

[26] A. K. Robinson, A. B. Artusio-Glimpse, M. T. Simons, and C. L. Holloway, Atomic spectra in a six-level scheme

for electromagnetically induced transparency and Autler-Townes splitting in Rydberg atoms, Phys. Rev. A **103**, 023704 (2021).

[27] H. Fan, S. Kumar, J. Sheng, J. P. Shaffer, C. L. Holloway, and J. A. Gordon, Effect of Vapor-Cell Geometry on Rydberg-Atom-Based Measurements of Radio-Frequency Electric Fields, Phys. Rev. Appl. **4**, 044015 (2015).

[28] D. A. Anderson, A. Schwarzkopf, S. A. Miller, N. Thaicharoen, G. Raithel, J. A. Gordon, and C. L. Holloway, Two-photon microwave transitions and strong-field effects in a room-temperature Rydberg-atom gas, Phys. Rev. A **90**, 043419 (2014).

[29] Y. Xue, Y. Jiao, L. Hao, and J. Zhao, Microwave two-photon spectroscopy of cesium Rydberg atoms, Opt. Express **29**, 43827 (2021).

[30] X.-H. Liu, K.-Y. Liao, Z.-X. Zhang, H.-T. Tu, W. Bian, Z.-Q. Li, S.-Y. Zheng, H.-H. Li, W. Huang, H. Yan, and S.-L. Zhu, Continuous-Frequency Microwave Heterodyne Detection in an Atomic Vapor Cell, Phys. Rev. Appl. **18**, 054003 (2022).

[31] P. R. Berman and V. S. Malinovsky, *Principles of Laser Spectroscopy and Quantum Optics* (Princeton University Press, Princeton, 2011).

[32] D. A. Steck, Cesium *D* line data, http://steck.us/alkalidata, revision 2.1.6, 20 September 2013 (1998).